POLITECNICO DI TORINO
Repository ISTITUZIONALE

Dynamic Landau–Khalatnikov Modeling of Ferroelectric Hafnium–Zirconium Oxides Across Volatile and NonVolatile Switching

Original
Dynamic Landau–Khalatnikov Modeling of Ferroelectric Hafnium–Zirconium Oxides Across Volatile and NonVolatile Switching / Rossetti, D., Xu, Y., Asapu, S., Moon, T., Kim, S.J., Austin, D.R., Zhao, R., Wang, T., Zhao, J., Everhart, B.M., Bonnin, M., Ascoli, A., Corinto, F., Glavin, N.R., Williams, R.S., Yang, J.J.. - In: ADVANCED ELECTRONIC MATERIALS. - ISSN 2199-160X. - ELETTRONICO. - (2026), pp. 1-14. [10.1002/aelm.70610]

Availability:
This version is available at: 11583/3016930 since: 2026-10-24T12:08:36Z

Publisher:
Wiley

Published
DOI:10.1002/aelm.70610

Terms of use:

This article is made available under terms and conditions as specified in the corresponding bibliographic description in the repository

Publisher copyright

(Article begins on next page)

19 November 2026

Check for updates

Advanced Electronic Materials

ADVANCED ELECTRONIC MATERIALS Open Access

www.advelectronicmat.de

RESEARCH ARTICLE OPEN ACCESS

Dynamic Landau–Khalatnikov Modeling of Ferroelectric Hafnium–Zirconium Oxides Across Volatile and Non-Volatile Switching

Davide Rossetti[1,2] | Yichun Xu[1] | Shiva Asapu[1] | Taehwan Moon[1] | Seung Ju Kim[1] | Drake R. Austin[3] | Ruoyu Zhao[1] | Tong Wang[1] | Jian Zhao[1] | Brian M. Everhart[3] | Michele Bonnin[2] | Alon Ascoli[2] | Fernando Corinto[2] | Nicholas R. Glavin[3] | R. Stanley Williams[1] | J. Joshua Yang[1]

[1]Department of Electrical and Computer Engineering, University of Southern California, Los Angeles, California, USA | [2]Department of Electronics and Telecommunications Engineering, Politecnico di Torino, Turin, Italy | [3]Materials and Manufacturing Directorate, Air Force Research Laboratory, Wright-Patterson AFB, Dayton, Ohio, USA

Correspondence: R. Stanley Williams (stan@rstanleywilliams.com) | J. Joshua Yang (jjoshuay@usc.edu)

Received: 27 April 2026 | **Revised:** 20 September 2026 | **Accepted:** 30 September 2026

Keywords: Edge AI | Ferroelectric Capacitor | Hafnium–Zirconium Oxide | Landau-Khalatnikov | Neuromorphic Computing | Non-Linear Dynamics

ABSTRACT

The design of energy-efficient neuromorphic devices demands compact, physically grounded models that seamlessly connect microscopic ferroelectric dynamics to macroscopic circuit behavior. Hafnium–zirconium oxides ($Hf_xZr_{1-x}O_2$, HZO) are compelling candidates owing to their CMOS compatibility, scalability below 10 nm, and tunable transition between ferroelectric and volatile responses. Yet, conventional first-order Landau–Khalatnikov (LK) formulations cannot capture key experimental features such as negative differential capacitance, pseudo-inductive transients, and leakage interplay. Here we introduce an extended LK framework incorporating inertial second-order terms, nonlinear charge-dependent damping, and a modular leakage branch. This unified, simulation-ready model quantitatively reproduces experimental Q–V characteristics across Hf-rich, equiatomic, and Zr-rich HZO compositions, defining operational regimes from non-volatile memory to volatile, reservoir-like dynamics. By linking free-energy landscapes to compact circuit representations, the approach establishes a predictive device–model–circuit co-design framework that connects atomistic energetics with system-level simulation, enabling composition-specific design rules for scalable, low-power neuromorphic architectures.

1 | Introduction

Neuromorphic computing has emerged as a leading strategy to overcome the energy and scalability bottlenecks of von Neumann architectures, demanding device primitives that are compact, energy-efficient, and functionally versatile [1, 2]. Within this context, ferroelectric devices offer distinct advantages over alternative material platforms, combining fast polarization dynamics with intrinsic non-volatility and thereby enabling memory and processing functions within a single physical unit [3–10]. Furthermore, expanding these multifunctional capabilities onto diverse and flexible platforms has driven the development of reconfigurable neuromorphic networks for ultra-low power applications [11]. Among ferroelectric systems, doped hafnium oxides have attracted sustained attention since the discovery of ferroelectricity in thin HfO_2 and $Hf_xZr_{1-x}O_2$ (HZO) films [12–16]. Their CMOS

Davide Rossetti and Yichun Xu contributed equally to this work.

This is an open access article under the terms of the Creative Commons Attribution License, which permits use, distribution and reproduction in any medium, provided the original work is properly cited.
© 2026 The Author(s). *Advanced Electronic Materials* published by Wiley-VCH GmbH

compatibility [17], excellent scalability, and robust switching behavior make them attractive for non-volatile memories [3, 4], negative differential capacitance field-effect transistors and oscillators [5, 6, 18], and energy-efficient logic applications [7]. Importantly, the composition parameter x in $HfxZr1-xO_2$ provides a powerful means of tuning the material's ferroelectric behavior: Hf-rich (x close to 1) films exhibit stable ferroelectric behavior with strong remanence, while Zr-rich (x close to 0) alloys approach volatile, field-induced ferroelectricity [19–21]. This compositional tunability unifies memory and dynamical processing functions within a single material family [22–25]. In parallel, leveraging such volatile and non-volatile transitions has opened up new pathways for advanced edge applications. Recent hardware-level innovations exploit these dynamic regimes for integrated near-sensor and in-sensor neuromorphic computing systems, implementing multi-level hardware security and secure encrypted information transmission [26, 27] Despite these advantages, predictive compact models for HZO-based devices remain limited. The canonical Landau–Khalatnikov (LK) formalism [28, 29], based on a first-order temporal derivative of polarization, has long served as the workhorse for describing ferroelectric hysteresis. Extensions of this framework have been used to capture volatile switching in fluorite oxides [24], and analytical procedures have been proposed for antiferroelectric ZrO_2 [30]. However, the overdamped LK model fails to reproduce key experimental signatures, including negative differential capacitance [31–33], oscillatory transients, pseudo-inductive effects [31], and the pronounced frequency–temperature dependence of leakage currents. Alternative approaches—such as Jiles–Atherton phenomenology [34], phase-field simulations with genetic optimization [35], and multi-domain models [36] incorporating charge trapping and interfacial defects [37]—have provided valuable insights but are often computationally demanding or lack transferability across compositions. Together, these studies reveal a critical gap: the lack of a computationally efficient approach that consistently links free-energy landscapes with nonlinear ferroelectric dynamics while remaining compatible with circuit-level simulation. Here, we introduce an extended Landau–Khalatnikov formulation that incorporates an inertial second-order derivative, nonlinear charge-dependent damping, and a modular leakage branch. The extended model quantitatively reproduces positive-up negative-down (PUND) and triangular-wave protocols across multiple HZO stoichiometries, revealing a composition phase diagram that spans non-volatile, partially volatile, and volatile regimes. Implemented in standard circuit simulators, the model enables co-simulation workflows that directly connect material composition with large-scale circuit performance, providing predictive guidelines for process optimization, electronic design automation (EDA) integration, and scalable deployment of energy-efficient ferroelectric devices in neuromorphic architectures.

2 | Results

2.1 | Device Fabrication and Characterization

A series of HZO capacitors with varying $Hf_xZr_{1-x}O_2$ compositions ($x = 0.8, 0.6, 0.5, 0.4, 0.2$) were fabricated in a metal–insulator–metal (MIM) configuration with a W/HZO/W stack. The HZO layers were grown by atomic layer deposition (ALD) to a thickness of ∼8 nm (80 cycles), with the precise $Hf_xZr_{1-x}O_2$ composition controlled by adjusting the ALD cycle ratio. X-ray photoelectron spectroscopy (XPS) confirmed that the resulting stoichiometry matched the intended recipes. Rapid thermal annealing (RTA) at 700°C for 20 s in forming gas (5% H_2 in N_2) was performed to obtain reproducible crystallization across all investigated $HfxZr1-xO_2$ compositions, providing a consistent experimental platform for compact-model extraction and validation [38–40].It is worth mentioning that the proposed modeling framework is independent of the specific annealing temperature and can be parameterized for HZO capacitors fabricated with different thermal budgets.

To verify the crystallographic phases and interface quality across the different HZO compositions, cross-sectional transmission electron microscopy (TEM) was performed directly on the patterned W/HZO/W capacitor stacks. Importantly, the cross-sectional TEM specimens were prepared from the same functional devices used in electrical measurements, ensuring that the observed microstructure corresponds to the actual operating environment. As shown in Figure 1a, the ∼8 nm HZO layer exhibits uniform thickness and clear interfaces with both the top and bottom W electrodes. The corresponding fast Fourier transform (FFT) pattern extracted from the HZO region reveals fluorite-derived diffraction features, including spots associated with orthorhombic and tetragonal symmetries. High-resolution synchrotron X-ray diffraction (XRD) was performed directly on the patterned W/HZO/W device stacks using a focused 15 μm × 125 μm beam at 9.7 keV and a 2° incidence angle. Importantly, the measurements were conducted on the actual functional capacitor structures rather than on blanket films. As shown in Figure 1b, the volatile $Hf_{0.2}Zr_{0.8}O_2$ composition exhibits a pronounced o(111)/t(101) feature near 30.5°, accompanied by a much weaker o(200)/c(200) reflection near 35.8° [41]. Together with its volatile, antiferroelectric-like electrical response, this diffraction profile is consistent with a predominantly tetragonal contribution to the 30.5° feature [42]. With increasing Hf content, the spectral weight near 30.5° decreases, whereas the o(200)/c(200) feature near 35.8° becomes substantially stronger. The enhancement of the latter accompanies the emergence of remanent polarization and well-defined ferroelectric hysteresis, supporting an increasing orthorhombic contribution in the Hf-rich samples. Because the two features contain overlapping o/t and o/c contributions, respectively, and may also be influenced by crystallographic texture, neither peak alone provides a quantitative measure of the orthorhombic-phase fraction. Nevertheless, their combined evolution, together with the electrical measurements, supports the composition-driven transition from predominantly tetragonal, volatile behavior to orthorhombic ferroelectric behavior. The diffraction peaks near 40.3° and 58.3° are assigned to the W(110) and W(200) reflections of the tungsten electrodes, respectively, and are clearly separated from the HZO reflections. Additional synchrotron XRD measurements comparing the complete $W/Hf_xZr_{1-x}O_2/W$ stack with regions where the top W electrode was removed (Figure S8) further demonstrate the critical role of the tungsten top electrode in stabilizing the orthorhombic phase during rapid thermal annealing. The substantial reduction of the o(200)/t(002) diffraction intensity after removal of the top electrode is consistent with the established understanding that the mechanical confinement and stress provided by the tungsten electrode

2199160x, 0, Downloaded from https://advanced.onlinelibrary.wiley.com/doi/10.1002/aelm.70610 by michele bonin - Politecnico Di Torino Sist. Bibl Del Polit Di Torino , Wiley Online Library on [24/10/2026]. See the Terms and Conditions (https://onlinelibrary.wiley.com/terms-and-conditions) on Wiley Online Library for rules of use; OA articles are governed by the applicable Creative Commons License

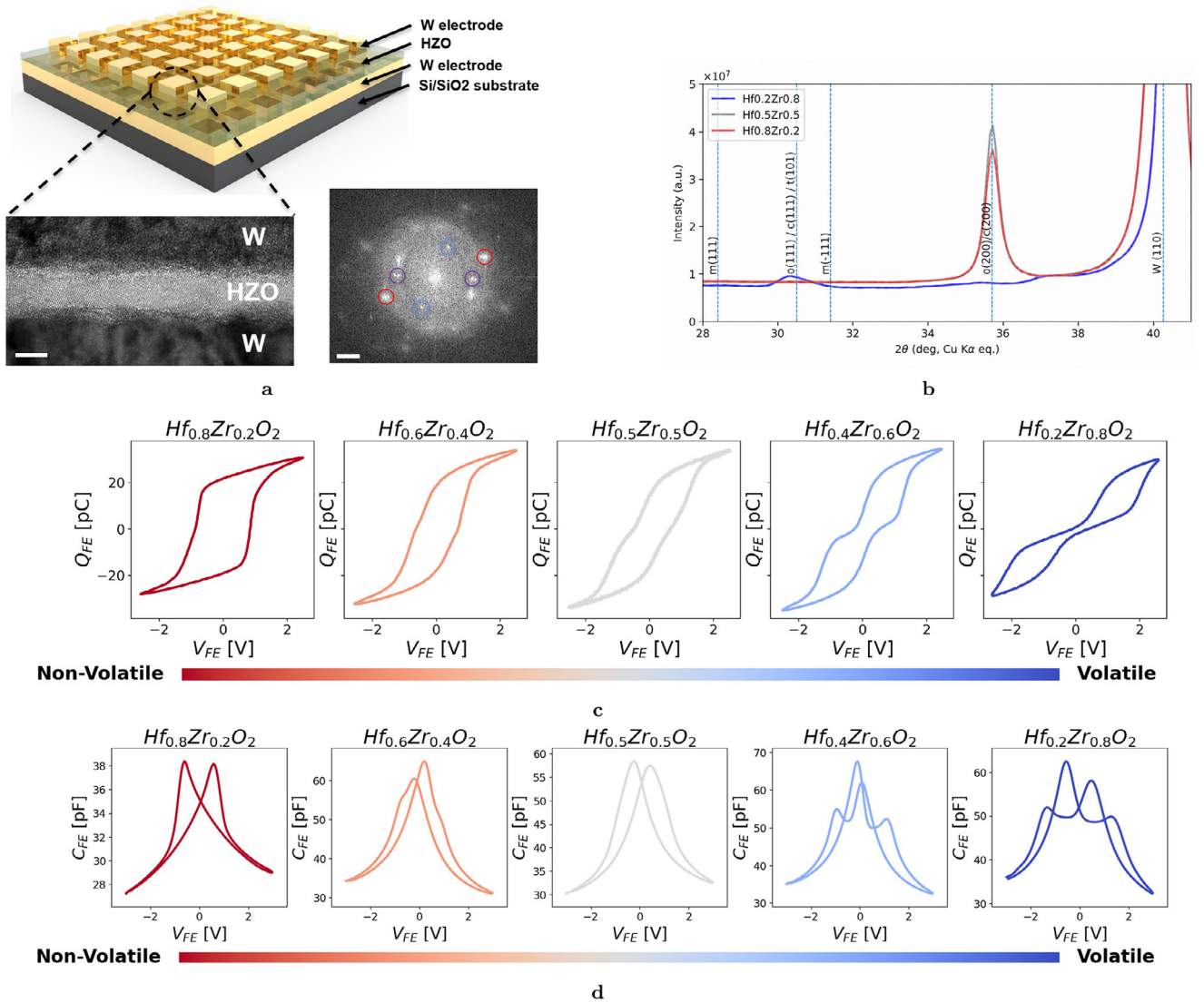


FIGURE 1 | Structural and electrical characterization of $Hf_xZr_{1-x}O_2$ capacitors. (a), Cross-sectional transmission electron microscopy (TEM) image of the W/$Hf_xZr_{1-x}O_2$/W capacitor stack, scale bar 5 nm. The inset shows the corresponding fast Fourier transform (FFT) pattern obtained from the HZO region, confirming the ferroelectic phase, scale bar 10 nm^{-1}. (b), Synchrotron XRD patterns of $Hf_xZr_{1-x}O_2$ capacitors with different compositions, illustrating the composition-dependent evolution of the crystalline phases. (c), Dynamic Q–V characteristics measured for different $Hf_xZr_{1-x}O_2$ compositions, demonstrating the transition from ferroelectric to antiferroelectric-like behavior with increasing Zr content. (d), *C–V* characteristics measured at 100 kHz for the corresponding devices.

promote formation of the metastable ferroelectric orthorhombic phase [15].

Charge–voltage (*Q–V*) loops were recorded using dynamic triangular inputs and PUND pulse schemes, with the triangular-wave measurements for the composition-dependent overview in Figure 1c acquired at 10 kHz after device stabilization and plotted as cycle-averaged experimental responses; capacitance–voltage (*C–V*) characteristics were measured at 100 kHz. As shown in Figure 1, the $Hf_{0.8}Zr_{0.2}O_2$ capacitor exhibits well-saturated ferroelectric hysteresis with a remanent polarization (P_r) of approximately 50 $\mu C\ cm^{-2}$, extracted at zero applied voltage after polarization switching. In contrast, the volatile $Hf_{0.2}Zr_{0.8}O_2$ capacitor displays the characteristic double hysteresis loop of antiferroelectric-like switching and does not exhibit a stable remanent polarization. Therefore, its polarization is characterized by the maximum polarization (*P*max) of approximately 75 $\mu C\ cm^{-2}$ reached during the voltage sweep. Intermediate compositions ($Hf_{0.6}Zr_{0.4}O_2$, $Hf_{0.5}Zr_{0.5}O_2$, $Hf_{0.4}Zr_{0.6}O_2$) revealed a continuous transition between these regimes. In $Hf_{0.6}Zr_{0.4}O_2$ and $Hf_{0.5}Zr_{0.5}O_2$, the ferroelectric and antiferroelectric-like transitions occur over partially overlapping voltage ranges, causing their capacitance peaks to merge. The individual contributions are more clearly resolved in $Hf_{0.6}Zr_{0.4}O_2$, whereas their stronger overlap in $Hf_{0.5}Zr_{0.5}O_2$ produces an apparently butterfly-like envelope. In contrast, $Hf_{0.8}Zr_{0.2}O_2$ exhibits a conventional ferroelectric butterfly response with a single dominant switching peak in each sweep direction and distinctly different peak voltages. These assignments are further supported by the Q–V characteristics, which more directly distinguish ferroelectric hysteresis from mixed and antiferroelectric-like switching. This compositional sweep provides a systematic dataset spanning the full

2199160x, 0, Downloaded from https://advanced.onlinelibrary.wiley.com/doi/10.1002/aelm.70610 by michele bonin - Politecnico Di Torino Sist. Bibl Del Polit Di Torino , Wiley Online Library on [24/10/2026]. See the Terms and Conditions (https://onlinelibrary.wiley.com/terms-and-conditions) on Wiley Online Library for rules of use; OA articles are governed by the applicable Creative Commons License

FE–VFE spectrum, which is essential for calibrating and validating the compact modeling framework. Endurance and retention tests confirmed that all devices maintained stable switching characteristics, ensuring the reliability of the extracted dynamic characteristics used for compact-model development. Detailed endurance and retention measurements of these HZO capacitors are reported in our previous work [43]. The demonstrated device stability provides a reliable basis for the compact-model parameter extraction performed in this work.

2.2 | Compact Circuit Model

A unified modeling framework is essential to benchmark key physical parameters, capture transient ferroelectric phenomena, and enable circuit-level simulations for next-generation neuromorphic architectures. The theoretical foundation for such systems, as emphasized in [24], is the Landau–Khalatnikov (LK) formalism, where the static polarization–electric field response is expressed through a polynomial expansion of the Landau–Ginzburg–Devonshire (LGD) free energy [28]. In its canonical form, the LGD theory retains only even-order terms, reflecting the centrosymmetric nature of the ideal ferroelectric lattice. However, real devices inevitably deviate from this symmetry due to built-in fields, electrode asymmetries, and defect distributions. To capture these non-idealities, odd-order contributions must be included, enabling faithful reproduction of experimentally observed asymmetries in the Q–V (or P–E) characteristics. The static free energy can thus be written as:

$$F(Q) = \left[\frac{1}{2}\alpha Q^2 + \frac{1}{4}\beta Q^4 + \frac{1}{6}\gamma Q^6 + \frac{1}{8}\delta Q^8\right] + \left[\frac{1}{3}\varphi Q^3 + \frac{1}{5}\zeta Q^5\right] - V_{FE}\cdot Q \quad (1)$$

where α, β, γ, and δ are the canonical LGD coefficients defining the symmetric double-well potential, while φ and ζ represent odd-order corrections that account for device-specific asymmetries. The external voltage V_{FE} couples linearly to the polarization, shifting the energy landscape. Physically, α governs the onset of ferroelectric instability (its sign determines whether the system is paraelectric, $\alpha > 0$, with a single minimum at $Q = 0$, or ferroelectric, $\alpha < 0$, with two symmetric minima at $\pm Q_r$). β and γ control the depth and curvature of the wells, while δ stabilizes the system at large polarization amplitudes. The odd-order terms tilt the potential, introducing asymmetry consistent with real device behavior. Together, these coefficients link the intrinsic material response to experimentally accessible quantities such as switching voltage, saturation and remanent charge, and the effective capacitance extracted from Q–V measurements. The electrical response of $Hf_xZr_{1-x}O_2$ (HZO) capacitors was modeled within an augmented Landau–Khalatnikov (L–K) framework. The conventional L–K formulation [28, 29, 44], limited to a first-order temporal derivative, describes only overdamped polarization dynamics and fails to reproduce the nonlinear transients observed experimentally. To overcome this limitation, we introduce an inertial second-order derivative that embeds pseudo-inductive behavior. Within the negative differential capacitance regime, this term renders the unstable branch repulsive, accelerating the trajectory's transit away from it (Section S9), and quantitatively captures overshoot and oscillatory features. The extended dynamics are expressed as:

$$Ldyn(Q)\frac{d^2Q}{dt^2} + R_{dyn}(Q)\frac{dQ}{dt} = -\frac{\partial F(Q)}{\partial Q} \quad (2)$$

where $L_{dyn}(Q)$ and $R_{dyn}(Q)$ are nonlinear functions of the charge Q, reflecting that both inertial and dissipative effects evolve with the ferroelectric state. Expanding the polynomial free-energy functional yields:

$$L_{dyn}(Q)\frac{d^2Q}{dt^2} + R_{dyn}(Q)\frac{dQ}{dt} = -[\alpha Q + \beta Q^3 + \gamma Q^5 + \delta Q^7] - [\varphi Q^2 + \zeta Q^4] + V_{FE} \quad (3)$$

with:

$$R_{dyn}(Q) = R_0 + R_1 Q + R_2 Q^2 + R_3 Q^3 \quad (4)$$

$$L_{dyn}(Q) = L_0 + L_1 Q + L_2 Q^2 + L_3 Q^3 \quad (5)$$

Here, $R_{dyn}(Q)$ defines the nonlinear damping landscape: R_0 quantifies the baseline ferroelectric switching dissipation, while R_1, R_2, and R_3 capture higher-order charge-dependent contributions from domain-wall motion and defect relaxation. In parallel, $L_{\mathrm{dyn}}(Q)$ represents an effective pseudo-inertial response of the ferroelectric polarization. Physically, this term accounts for the finite-time evolution of the polarization state during switching: the macroscopic charge does not follow the applied electric field instantaneously, but evolves with a delay associated with collective polarization reversal. This inertial contribution depends strongly on the charge Q flowing through the capacitor, since different values of Q correspond to different positions along the switching trajectory. L_{dyn} is modeled as a charge-dependent function, with L_0 describing the baseline pseudo-inertial response and L_1, L_2, and L_3 describing its nonlinear evolution with charge. By elevating both R_{dyn} and L_{dyn} to charge-dependent expansions, the model goes beyond a purely phenomenological description and provides a physically transparent compact representation of state-dependent dissipation and pseudo-inertial polarization dynamics [24, 31]. We emphasize that the present formulation cannot be reduced to a first-order LK model supplemented by a single linear R–L branch. A constant resistance and inductance can only introduce a uniform phase delay, whereas the measured Q–V trajectories require dissipative and pseudo-inertial contributions that evolve with the polarization state. Moreover, forcing a first-order LK model to fit the ferroelectric compositions leads to an unphysical positive α coefficient, corresponding to a single-well free-energy landscape despite the experimentally observed remanent polarization. The charge-dependent $L_{\mathrm{dyn}}(Q)$, including its effective negative values within the NDC region, is therefore essential to retain a physically consistent double-well Landau landscape, as shown in Figure 4. Rearranging Equation (3), the voltage across the ferroelectric device can be written as:

$$v_{FE}(Q) = L_{dyn}(Q)\frac{d^2Q}{dt^2} + R_{dyn}(Q)\frac{dQ}{dt} + f(Q) \quad (6)$$

2199160x, 0, Downloaded from https://advanced.onlinelibrary.wiley.com/doi/10.1002/aelm.70610 by michele bonin - Politecnico Di Torino Sist. Bibl Del Polit Di Torino , Wiley Online Library on [24/10/2026]. See the Terms and Conditions (https://onlinelibrary.wiley.com/terms-and-conditions) on Wiley Online Library for rules of use; OA articles are governed by the applicable Creative Commons License

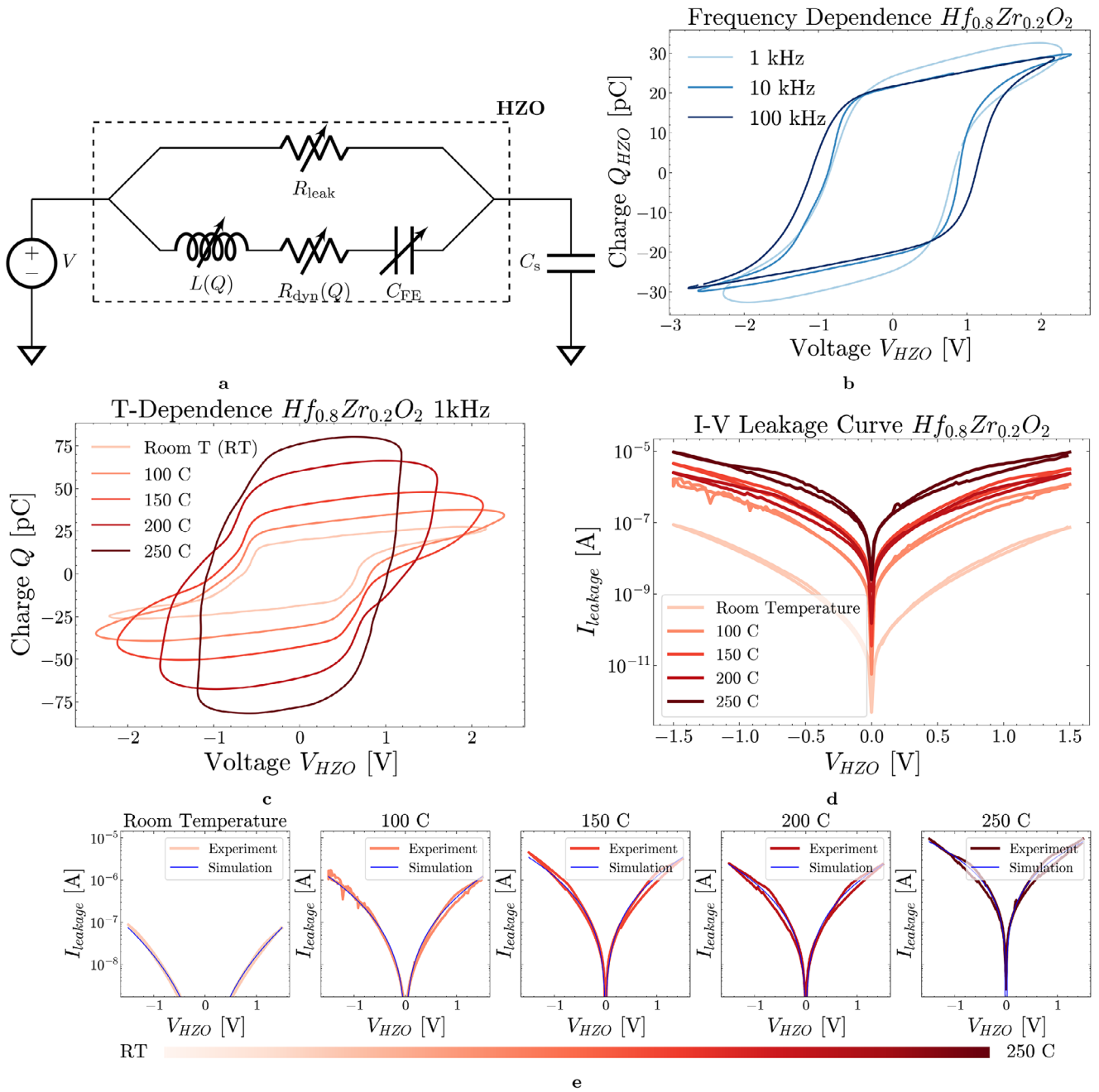


FIGURE 2 | Circuit model, frequency/temperature-dependent Q–V response, and leakage analysis of Hf-rich HZO ($Hf_{0.8}Zr_{0.2}O_2$). (a), Equivalent compact-model topology, consisting of a second-order Landau–Khalatnikov core in parallel with a nonlinear Poole–Frenkel leakage branch. (b), Dynamic charge–voltage (Q–V) loops measured as a function of triangular-wave drive frequency from 1 to 100 kHz. (c), Temperature-dependent Q–V loops measured from room temperature to 250°C, showing the increasing contribution of thermally activated leakage at elevated temperature. (d), Experimental leakage-current characteristics revealing thermally activated field-assisted conduction. (e), Poole–Frenkel leakage-branch fits to the experimental leakage curves at each temperature (experiment in red, model in blue).

where the static nonlinear term is defined as:

$$f(Q) = \alpha Q + \beta Q^3 + \gamma Q^5 + \delta Q^7 + \varphi Q^2 + \zeta Q^4 \qquad (7)$$

Here, $f(Q)$ governs the static Q–V response and can be interpreted as the effective restoring force of the ferroelectric lattice, i.e., the contribution of the ferroelectric capacitance C_{FE} in the equivalent circuit of Figure 2a. In contrast, the additional dynamic terms $L_{dyn}(Q)$ and $R_{dyn}(Q)$ encode the non-equilibrium processes. This decomposition, schematized in Figure 2a, highlights how the extended LK framework unifies static thermodynamic stability (through $f(Q)$) with dynamic relaxation and inertial phenomena (through $R_{dyn}(Q)$ and $L_{dyn}(Q)$), providing a direct path from free-energy landscapes to experimentally observed transient signatures. Beyond conceptual clarity, the circuit formulation enables quantitative fitting of Q–V characteristics across frequencies, reproducing with high fidelity the experimental trends shown in Figure 2b (see Section S1 for

2199160x, 0, Downloaded from https://advanced.onlinelibrary.wiley.com/doi/10.1002/aelm.70610 by michele bonin - Politecnico Di Torino Sist. Bibl Del Polit Di Torino , Wiley Online Library on [24/10/2026]. See the Terms and Conditions (https://onlinelibrary.wiley.com/terms-and-conditions) on Wiley Online Library for rules of use; OA articles are governed by the applicable Creative Commons License

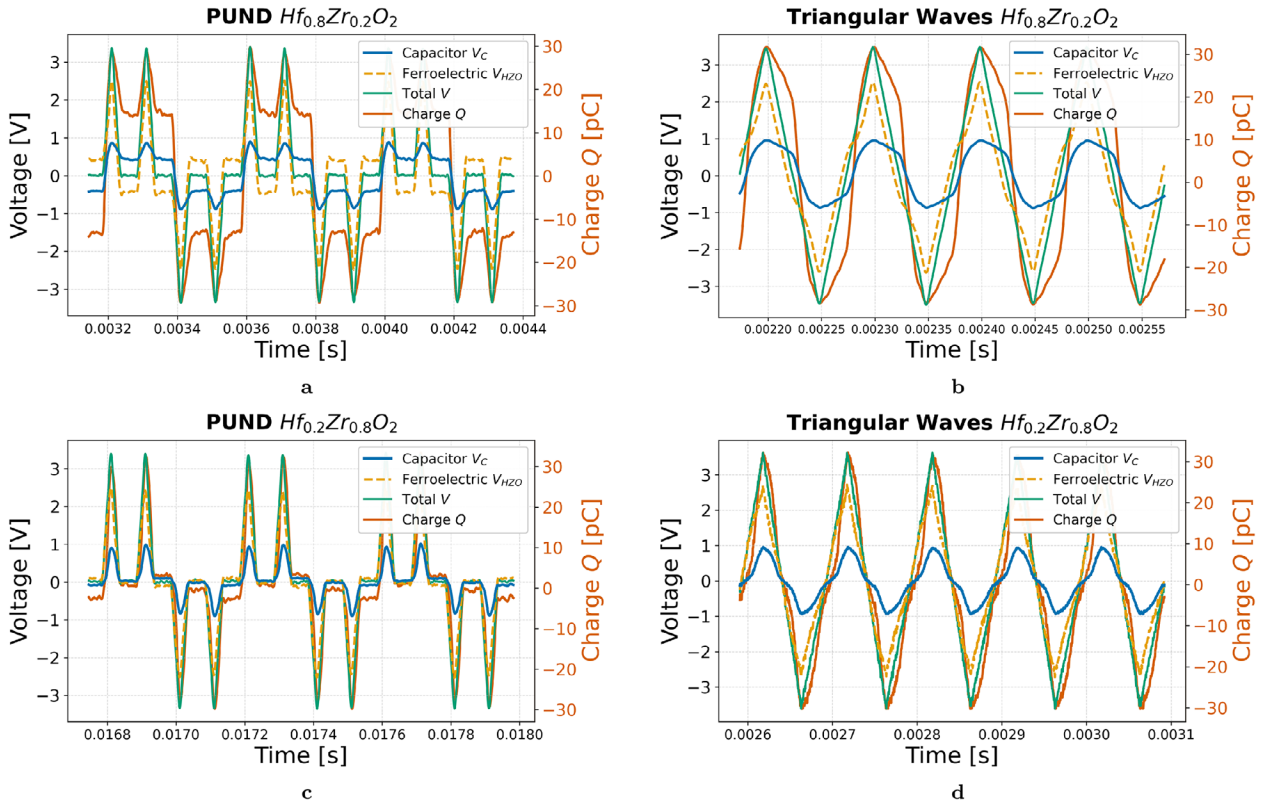


FIGURE 3 | Experimental PUND and triangular-wave measurements of $Hf_{0.8}Zr_{0.2}O_2$ and $Hf_{0.2}Zr_{0.8}O_2$. (a), PUND measurements on $Hf_{0.8}Zr_{0.2}O_2$, demonstrating stable remanent polarization. (b), Triangular-wave measurements on $Hf_{0.8}Zr_{0.2}O_2$. (c), PUND measurements on $Hf_{0.2}Zr_{0.8}O_2$, showing negligible remanent polarization. (d), Triangular-wave measurements on $Hf_{0.2}Zr_{0.8}O_2$. *Color legend (all panels)*: orange, charge Q; green, total circuit voltage V; yellow dashed, ferroelectric voltage V_{HZO}; blue, voltage across the linear capacitor V_C.

other HZO compositions). At high frequency, the response is dominated by intrinsic ferroelectric switching and the inertial stabilization provided by $L_{dyn}(Q)$, yielding sharp transients and minimal distortion. At lower frequency or under quasi-static conditions, however, leakage currents [45, 46] become increasingly prominent, modifying the apparent hysteresis and even partially masking the underlying ferroelectric features. The inclusion of a Poole–Frenkel [47] branch in the compact model is therefore essential to capture the strong temperature and field dependence of the leakage, which reshapes the Q–V profile as observed experimentally in Figure 2c (higher zirconium compositions are further detailed in Section S2 [48, 49]). Thus, the extended LK model captures intrinsic polarization dynamics while disentangling the interplay between reversible switching and dissipative leakage channels, enabling a physically grounded interpretation of frequency- and temperature-dependent signatures. The Poole–Frenkel (PF) leakage process involves field-assisted emission of carriers from trap states into the conduction band [50], which reduces the barrier height Φ_B and leads to a current that scales as:

$$I_{\text{leak}}(f,T) \propto E \exp\left[-\frac{\Phi_B - \sqrt{\frac{qE}{\pi\epsilon}}}{k_B T}\right] Y(f) \simeq I_0(T,f)\exp\left[\beta(T)\sqrt{V}\right] \tag{8}$$

where ϵ is the dielectric permittivity, while $I_0(T,f)$ and $\beta(T)$ are functions of the temperature T encapsulating the field- and material-dependent prefactors. Thus, Φ_B represents an effective trap-depth/barrier for field-assisted emission from Coulombic defect states [45, 51, 52]. In the compact implementation used here, Φ_B is incorporated into the effective prefactor $I_0(T,f)$, together with trap density, attempt frequency, dielectric response, thickness-dependent factors, and other material-dependent contributions. This reduced representation preserves the experimentally observed dependence on electric field and temperature while keeping the leakage branch compact and directly compatible with circuit-level simulation. In practice, the square-root exponential dependence on the applied voltage dominates the weaker linear prefactor. The Poole–Frenkel pathway exhibits a pronounced temperature sensitivity (Figure 2d,e), consistent with its thermally activated nature, and a frequency dependence that reflects the finite response time of trap states. The PF model quantitatively reproduces the quasi-static current–voltage experimental data, as shown by the excellent agreement between the red experimental traces and the blue simulation curves in Figure 2e. This agreement extends across different temperatures, underscoring the robustness of the formulation. Furthermore, the frequency dependence of the leakage current follows a Lorentzian-like behavior, as detailed in Section S3, reflecting the characteristic relaxation dynamics of trap-mediated conduction. Model parameters were quantitatively extracted by fitting the experimental Q–V loops across frequencies and compositions, ensuring numerical consistency between simulation and experiment (see Methods for details). In a rigorous Landau description, temperature modifies not only the leakage

2199160x, 0, Downloaded from https://advanced.onlinelibrary.wiley.com/doi/10.1002/aelm.70610 by michele bonin - Politecnico Di Torino Sist. Bibl Del Polit Di Torino , Wiley Online Library on [24/10/2026]. See the Terms and Conditions (https://onlinelibrary.wiley.com/terms-and-conditions) on Wiley Online Library for rules of use; OA articles are governed by the applicable Creative Commons License

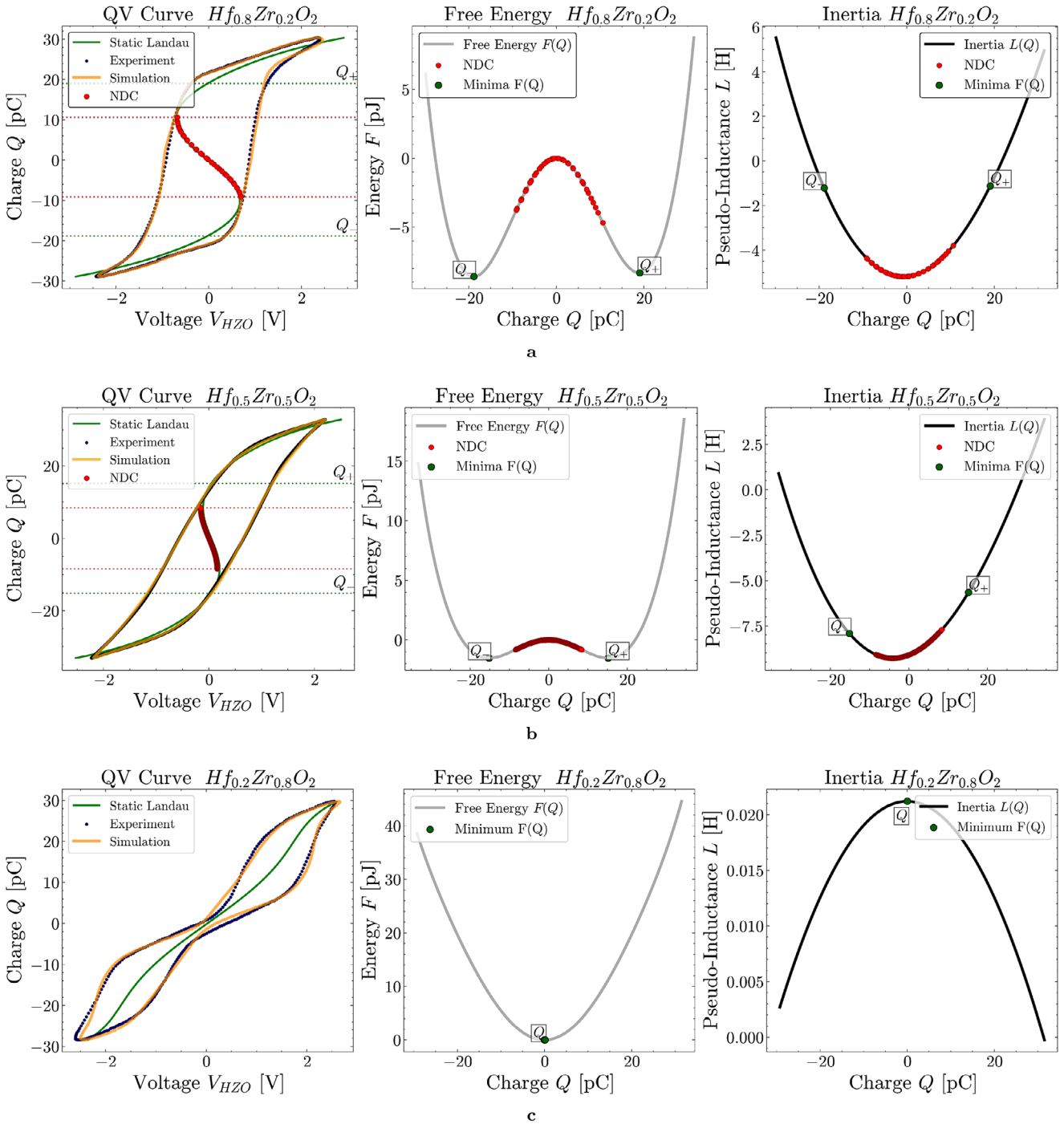


FIGURE 4 | Composition-dependent Q–V, free-energy, and inertial profiles. Each panel (a–c) contains three subplots: *left*, dynamic Q–V loops with the circuit simulation (orange line) overlaid on the experiment (blue dots) and the static Landau response (green line); *middle*, the corresponding free-energy profile $F(Q)$; *right*, the pseudo-inductance (inertia) landscape. Red dots mark regions associated with static negative differential capacitance (NDC), whereas green dots indicate the minima of the free energy, corresponding to stable polarization states Q_+ and Q_-. (a), $Hf_{0.8}Zr_{0.2}O_2$ (Hf-rich): deep double-well $F(Q)$ and inertia with upward concavity. (b), $Hf_{0.5}Zr_{0.5}O_2$ (equiatomic): shallower double-well $F(Q)$ with attenuated hysteresis and a weaker inertia signature. (c), $Hf_{0.2}Zr_{0.8}O_2$ (Zr-rich): single-well (approximately parabolic) $F(Q)$ and inertia with downward concavity.

current but also the ferroelectric free-energy landscape, the LGD coefficients, and the dynamic terms $R_{dyn}(Q)$ and $L_{dyn}(Q)$. Therefore, a predictive high-temperature LK+PF transient simulation cannot be obtained by simply adding a temperature-dependent PF branch to a fixed room-temperature LK core. Such a simulation would require re-extraction of the complete parameter set at each temperature. For this reason, our modeling strategy separates two well-defined operating regimes: (i) room-temperature, moderate-to-high-frequency measurements, where leakage is minimized and the intrinsic extended-LK response is isolated, and (ii) low-frequency or high-temperature measurements, where thermally activated PF leakage becomes prominent and modifies the apparent hysteresis. This approach avoids an artificial decomposition of the measured charge response

2199160x, 0, Downloaded from https://advanced.onlinelibrary.wiley.com/doi/10.1002/aelm.70610 by michele bonin - Politecnico Di Torino Sist. Bibl Del Polit Di Torino , Wiley Online Library on [24/10/2026]. See the Terms and Conditions (https://onlinelibrary.wiley.com/terms-and-conditions) on Wiley Online Library for rules of use; OA articles are governed by the applicable Creative Commons License

while preserving the physical consistency of the compact-model parameters.

The extracted leakage parameters were incorporated into the complete compact model together with the nonlinear Landau–Khalatnikov dynamics. The resulting Cadence simulations quantitatively reproduce the experimentally measured dynamic Q–V characteristics over the investigated composition range, as shown in Figure 4 and Figure S7. In addition, the same parameter set accurately captures both the PUND and triangular-wave measurement protocols (Figure 3; Section S4), demonstrating the consistency of the proposed modeling framework across different electrical characterization methods.

2.3 | Energy Landscape and Dynamics

To disentangle the static and dynamic contributions governing HZO capacitors, we combined two complementary experimental protocols. The PUND scheme (Figure 3a,c) was first employed to selectively extract the switchable polarization by suppressing dielectric and leakage contributions, whereas triangular voltage waveforms (Figure 3b,d) were used to directly trace the time evolution of charge and voltage under cyclic excitation. Both approaches were implemented within the circuit of Figure 2a, consisting of a voltage source (V) driving an in-house fabricated HZO device (V_{HZO}) in series with a 33 pF linear capacitor (V_C). The series capacitor stabilizes the overall dynamics and ensures operation deep in the regime where ferroelectric nonlinearity and instability are most pronounced.

This configuration reveals striking composition-dependent differences. In $Hf_{0.8}Zr_{0.2}O_2$, the charge stored in the series branch remains close to ±15 pC at $V = 0$, unambiguously indicating multiple remanent states and robust non-volatile behavior (Figure 3a). By contrast, $Hf_{0.2}Zr_{0.8}O_2$ exhibits no discernible memory, aside from a minor residual charge after the second pulse that is insufficient to define stable polarization states (Figure 3c). The triangular-wave measurements further emphasize this dichotomy: $Hf_{0.8}Zr_{0.2}O_2$ displays smooth, rounded Q–V trajectories typical of stable ferroelectric switching, whereas the volatile $Hf_{0.2}Zr_{0.8}O_2$ device shows sharp, discontinuous features reflecting its rapid return to a single equilibrium configuration. Importantly, these experimental observations are fully consistent with the Cadence circuit simulations (Section S4 and Figure S10), which accurately reproduce both the PUND transient responses and the triangular-wave measurements using a single set of extracted model parameters. This agreement confirms that the extracted memory characteristics originate from the intrinsic ferroelectric dynamics captured by the proposed compact model rather than from parasitic artifacts. The combined use of triangular-wave and PUND protocols therefore provides a comprehensive quantification of both reversible dielectric and irreversible ferroelectric switching components, mapping the transition between volatile and non-volatile regimes in $Hf_xZr_{1-x}O_2$ capacitors [3, 24, 53, 54]. These results call for a microscopic description linking remanent memory to dynamical volatility. We therefore move from direct measurements to a free-energy landscape analysis, coupled with circuit-level simulations, to reveal how the intrinsic energetics of HZO dictate the experimentally observed behaviors. The stability of ferroelectric capacitors is governed by their free-energy landscape: in standard hafnium–zirconium oxide ($Hf_{0.5}Zr_{0.5}O_2$), the archetypal double-well profile hosts two minima at $Q_\pm$ (remanent polarization), separated by a central maximum corresponding to the unstable paraelectric state. Positive curvature of the free-energy profile at the minima ($d^2F/dQ^2 > 0$) ensures thermodynamic stability, whereas negative curvature at the barrier ($d^2F/dQ^2 < 0$) corresponds to an unstable regime that manifests experimentally as negative differential capacitance (NDC). In practice, NDC appears as a negative slope in the static Q–V characteristic ($dQ/dV < 0$), as shown in the first column of Figure 4; by contrast, time-domain Q–V transients measured using the circuit of Figure 2a probe how trajectories approach, traverse, and relax from this unstable region. Standard first-order (overdamped) Landau–Khalatnikov models cannot reproduce the inertia-like overshoot [55–57] and damped oscillations observed near the barrier. Extending the LK framework with a pseudo-inductive channel $L_{dyn}(Q)$, acting together with the charge-dependent dissipation $R_{dyn}(Q)$, reproduces the observed overshoot and damped oscillations as the trajectory transits the $d^2F/dQ^2 < 0$ sector.

This extension quantitatively accounts for the observed overshoot and demonstrates how NDC can be dynamically harnessed in circuits, sustaining charge plateaus at $V = 0$. To make this connection quantitative, we combined analytical fitting and circuit co-simulation. Experimental charge traces were first denoised using a Savitzky–Golay filter in Python, tuning the polynomial order and window length to suppress noise while preserving physical curvature. Nonlinear regression was then used to extract initial Landau coefficients by matching the experimental dynamic Q–V loops (see Methods for details). The parameters were refined through Cadence simulations until convergence of both the loop area and remanent charge was achieved. Acquisition at 10 kHz minimized leakage contributions and isolated the intrinsic ferroelectric nonlinearity, enabling a single self-consistent description that reproduces both the measured memory charge at V=0 and the shape of the Q–V loops with $R^2 > 0.99$ across all compositions.

2.4 | Charge-Dependent Dynamic Resistance and Dissipation

While the free-energy landscape defines the static thermodynamic stability and the extended Landau–Khalatnikov framework captures the dynamical trajectories, the dissipative channel encoded in the charge-dependent resistance $R_{dyn}(Q)$ provides direct insight into how energy is locally dissipated during switching. To elucidate this aspect, we analyze the dynamic resistance together with the corresponding dissipated power as functions of charge (Figure 5). A clear compositional dependence emerges. For the Hf-rich composition ($Hf_{0.8}Zr_{0.2}O_2$), the behavior indicates that energy dissipation is strongly localized around the switching region, where domains are actively reversing, whereas in the saturated states the system becomes dynamically more rigid and dissipative processes are suppressed. In contrast, the equimolar composition ($Hf_{0.5}Zr_{0.5}O_2$) exhibits enhanced effective damping in the central region, consistent with strong domain-wall motion and interactions. As the system approaches saturation, both the resistance and the dissipated power decrease, reflecting the progressive reduction of competing switching processes. A

2199160x, 0, Downloaded from https://advanced.onlinelibrary.wiley.com/doi/10.1002/aelm.70610 by michele bonin - Politecnico Di Torino Sist. Bibl Del Polit Di Torino , Wiley Online Library on [24/10/2026]. See the Terms and Conditions (https://onlinelibrary.wiley.com/terms-and-conditions) on Wiley Online Library for rules of use; OA articles are governed by the applicable Creative Commons License

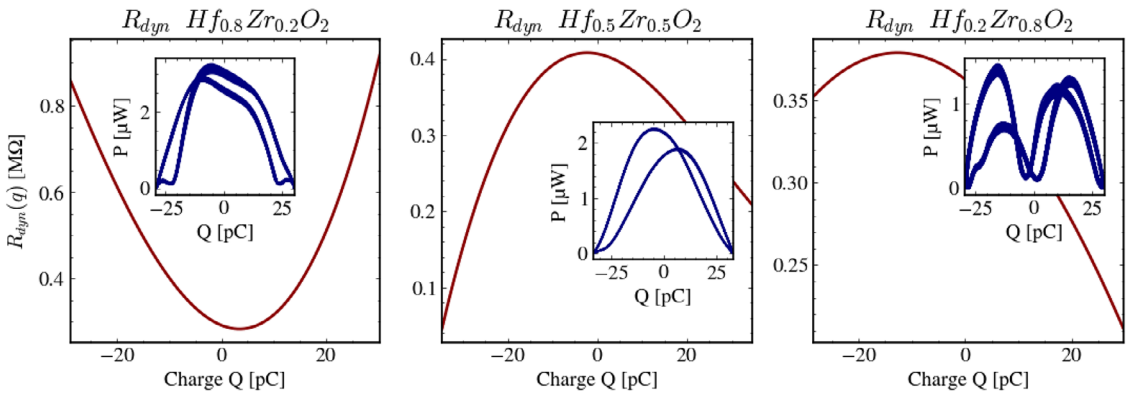


FIGURE 5 | Charge-dependent dynamic resistance and dissipated power across HZO compositions. Each panel (a–c) shows the dynamic resistance $R(q)$ as a function of charge (main axes), with the corresponding dissipated power $P(q)$ reported in the inset. Together, these quantities highlight how energy dissipation is distributed along the charge cycle. (a), $Hf_{0.8}Zr_{0.2}O_2$: minimum of $R(q)$ near $q \approx 0$ and monotonic increase toward larger $|q|$, with $P(q)$ concentrated around the central region. (b), $Hf_{0.5}Zr_{0.5}O_2$: peak of $R(q)$ at $q \approx 0$ and reduced values toward saturation, with a corresponding central maximum in $P(q)$. (c), $Hf_{0.2}Zr_{0.8}O_2$: smooth and asymmetric $R(q)$ profile, while $P(q)$ exhibits multiple peaks distributed over the charge range.

qualitatively different regime is observed in the Zr-rich composition ($Hf_{0.2}Zr_{0.8}O_2$). In this case, dissipation is distributed across the charge range and does not directly map onto the features of $R_{dyn}(Q)$, indicating that it is strongly influenced by the nonlinear and hysteretic current dynamics. This behavior suggests a more distributed and continuous switching process, rather than a sharply localized dissipative event. Overall, these results show that the charge-dependent dynamic resistance provides an experimentally accessible window into the dissipative mechanisms of ferroelectric switching, complementing the information obtained from the static free-energy landscape. In this framework, $R_{dyn}(Q)$ emerges not merely as a fitting parameter, but as a physically meaningful descriptor of the underlying switching dynamics. In addition, a numerical and analytical analysis demonstrates that, within experimentally extracted parameter regimes, HZO capacitors do not exhibit self-sustained oscillatory behavior, while oscillations can only arise under unphysical parameter conditions within the same second-order framework (Section S8).

2.5 | Compositional Control of Ferroelectric Dynamics

Varying the Hf/Zr ratio (Figure 4) directly reshapes both the free-energy landscape and device dynamics. For $Hf_{0.8}Zr_{0.2}O_2$ (Hf-rich), the landscape displays deep double wells with a wide static NDC interval ($dQ/dV < 0$, equivalently $[df(Q)/dQ]^{-1} < 0$). Within the second-order Landau–Khalatnikov framework, the charge-dependent pseudo-inductance $L_{dyn}(Q)$ becomes negative precisely across the NDC segment, speeding the departure from the barrier toward the neighboring free-energy minimum (Section S9). This sign structure shapes the trajectory as it escapes the unstable region and settles into the minima. In our fits, $L_{dyn}(Q)$ reaches its minimum (negative value, maximum in magnitude) near the local free-energy barrier, and crosses zero near the bottoms of the wells where the curvature is positive. This sign structure slows and regularizes the trajectory as it traverses the unstable region and releases it as it settles into the minima. Consequently, the Q–V loops are smooth and rounded, with robust remanence (±20 pC at V=0), consistent with the state settling into the free-energy minima (Figure 4a). The equiatomic composition $Hf_{0.5}Zr_{0.5}O_2$ (Figure 4b) lies between the non-volatile Hf-rich and volatile Zr-rich limits. Its free-energy landscape retains a double-well topology, yet the wells are markedly shallower than in $Hf_{0.8}Zr_{0.2}O_2$. Within the second-order LK picture, $L_{dyn}(Q)$ maintains the same sign structure—negative across the NDC segment and crossing zero near the minima—thus still regularizing the passage through the unstable branch. However, the comparable Hf and Zr contributions redistribute the dynamic weights, yielding a stronger and more diffuse inertial peak near the barrier. Accordingly, the behavior is intermediate, with enhanced dispersion relative to $Hf_{0.8}Zr_{0.2}O_2$ (see Section S5 for intermediate compositions: $Hf_{0.6}Zr_{0.4}O_2$ and $Hf_{0.4}Zr_{0.6}O_2$). By contrast, the Zr-rich $Hf_{0.2}Zr_{0.8}O_2$ (Figure 4c) exhibits a single-minimum free-energy profile within the same bias window. In this regime, $L_{dyn}(Q)$ is much smaller in magnitude—effectively negligible on the scale of the device dynamics—and remains strictly positive across the accessible charge range. Its profile is concave-down, opposite to the concave-up peak accompanying the NDC segment in Hf-rich and equiatomic samples. With the NDC interval largely suppressed, the transient responses become sharp and volatile, lacking stable remanence. Even when an apparent NDC-like slope emerges under high drive in the Zr-rich samples, it does not correspond to a genuine inversion of free-energy curvature, no double-well formation, consistent with recent analyzes [3, 24]. This evolution, captured by the extended LK formulation, directly links the material's free-energy landscape to its computational representation.

3 | Discussion

The dynamical channel in HZO capacitors emerges as a genuine design parameter rather than a descriptive add-on. The free-energy landscape provides the backdrop, but the functional response is governed by the balance between inertia, captured by the pseudo-inductance $L_{dyn}(Q)$, and dissipation, represented by $R_{dyn}(Q)$. In this context, the charge-dependent dynamic resistance provides direct access to how dissipation is distributed along the switching trajectory. As shown in Figure 5, energy losses are not uniform in charge but become strongly localized or distributed depending on composition, revealing distinct

2199160x, 0, Downloaded from https://advanced.onlinelibrary.wiley.com/doi/10.1002/aelm.70610 by michele bonin - Politecnico Di Torino Sist. Bibl Del Polit Di Torino , Wiley Online Library on [24/10/2026]. See the Terms and Conditions (https://onlinelibrary.wiley.com/terms-and-conditions) on Wiley Online Library for rules of use; OA articles are governed by the applicable Creative Commons License

dissipative regimes that are not directly inferred from the static free-energy landscape alone. To retain the physics of a nonlinear, history-dependent device, both quantities are modeled as explicit functions of charge: $R_{dyn}(Q)$ and $L_{dyn}(Q)$ evolve with the polarization state as domains nucleate, walls move, defects reconfigure, and leakage pathways activate. Treating them as constants, as commonly done in simplified circuit representations, would suppress these couplings and obscure the pseudo-inductive features of switching. We identify L_{dyn} as an effective order parameter: negative L_{dyn} overlapping static NDC accelerates the transit through the unstable branch, enabling non-volatile operation in Hf-rich material; small positive L_{dyn} yields volatile, fast-relaxing responses in Zr-rich material. This transient, state-dependent sign change remains fully compatible with global passivity of the device (Section S10).

In particular, the red dots in Figure 4 indicate regions associated with static negative differential capacitance (NDC). In this regime, the free-energy profile exhibits a local maximum, corresponding to the unstable polarization states, while the pseudo-inductance reaches its largest negative magnitude. This negative inductive contribution compensates the NDC behavior by rendering the barrier region repulsive along every direction (Section S9), which damps the tendency of the trajectory to rebound back over it after an abrupt switching event. The inertial contribution varies strongly with composition. This compositional dependence is mirrored in the dissipative channel, where the structure of $R_{dyn}(Q)$ and the associated power dissipation highlight a transition from localized switching losses in Hf-rich systems to more distributed and nonlinear dissipation in Zr-rich compositions. Hf-rich alloys retain deep double wells and switch rigidly with minimal overshoot, while Zr-rich films approach the volatile ZrO_2 limit, where frequency-dependent resistance dominates and inertia is suppressed. Intermediate stoichiometries ($Hf_{0.5}Zr_{0.5}O_2$, $Hf_{0.6}Zr_{0.4}O_2$, $Hf_{0.4}Zr_{0.6}O_2$; Section S5) exhibit the strongest pseudo-inductive peak, with large negative L_{dyn}—a fingerprint of marginal stability in a flattened double well, where small charge perturbations drive large voltage excursions. This yields a pronounced inertial effect at intermediate compositions, consistent with ultrafast polarization switching in HZO [58–60]. From an engineering standpoint, these regimes define a composition–based phase diagram. Hf-rich capacitors suit non-volatile storage at V=0, consistent with the hafnia platform and its CMOS trajectory [12]. Equiatomic devices trade full remanence for controllability and bandwidth, enabling (i) dynamic capacitive synapses with tunable short-term plasticity or "timer" behavior [61, 62], and (ii) capacitive neurons with tunable threshold and leaky integration—neurons with memory through co-localized integration and a semi-persistent state [63–65]. The same controllable partial remanence also supports logic-in-memory and polymorphic or reconfigurable logic (e.g., runtime NAND ↔ NOR, camouflaged logic) in compact FeFET/AFeFET cells [66–69]. Under appropriate stacks, phase-lead or negative differential capacitance windows further enable adaptive filtering and relaxation oscillators with wide tuning [5, 6, 70, 71]. Zr-rich devices exhibit volatile high-speed dynamics ideally suited for reservoir computing and temporal signal processing, as demonstrated in all-ferroelectric and HZO-based reservoirs [72, 73]. On the modeling side, the modularity of the framework ensures predictive transferability. Co-fitting $f(Q)$, $R_{dyn}(Q)$, $L_{dyn}(Q)$, and the leakage branch allows experimental protocols (e.g., PUND, stabilized triangular sweeps) to disentangle reversible and dissipative channels. The Poole–Frenkel branch captures activation trends and can be replaced by Schottky, tunneling, or SCLC pathways without altering the second-order LK core. This dual perspective, composition-tuned phenomenology combined with a modular compact model, offers a coherent route from fundamental switching dynamics to predictive computational design of ferroelectric devices. The present compact model describes the electrical behavior of HZO capacitors for a given device state. Extending the framework to incorporate cycle-dependent parameter evolution associated with wake-up, fatigue, and long-term degradation represents an important direction for future compact-model development.

4 | Conclusion

We introduced a second order dynamic extension of the Landau–Khalatnikov (LK) framework that connects free-energy landscapes to measured nonlinear device and circuit responses through a compact, simulation-ready formulation calibrated across compositions, frequencies, and temperatures. The model reveals how the interplay between inertial and dissipative channels governs the stabilization or suppression of transient negative differential capacitance. At the materials–device level, surveying five Hf–Zr stoichiometries uncovers a graded composition–based landscape that clusters into three operational archetypes: (i) Hf-rich stacks with deep double wells and robust, low-power states; (ii) intermediate mixtures with attenuated bistability and partial volatility; and (iii) Zr-rich stacks with sharp, volatile dynamics. These regimes provide actionable design rules for selecting chemistries and operating windows that minimize energy consumption while preserving state fidelity. Methodologically, the work establishes a consistent framework for benchmarking and co-simulating ferroelectric devices that integrates leakage transport and circuit parasitics while remaining transferable across material stacks. Embedding the compact model within process-design and electronic-design-automation flows will enable predictive circuit exploration and silicon validation through NC-assisted amplifiers, sense elements, and cross-point arrays. Incorporating multidomain kinetics and stochastic switching will further extend the framework toward variability-aware compact modeling. Together, these developments outline a predictive path from material energetics to deployable analog primitives for low-power, compute-in-memory architectures.

5 | Experimental Section

5.1 | Device Fabrication and Measurement

A series of HZO capacitors with varying $Hf_xZr_{1-x}O_2$ compositions (x = 0.8, 0.6, 0.5, 0.4, 0.2) were manufactured in a metal-insulator-metal (MIM) configuration with a W/HZO/W stack. The fabrication process began with the deposition of a 30 nm-thick W bottom electrode on Si/SiO_2 substrates by DC sputtering. The HZO layers were grown by atomic layer deposition (ALD) to a thickness of ∼8 nm (80 cycles). Compositional differences in HZO are controlled by the Hf-to-Zr layer numbers during ALD. A 30 nm-thick W top electrode was then deposited and patterned by photolithography and liftoff. Rapid thermal annealing (RTA)

2199160x, 0, Downloaded from https://advanced.onlinelibrary.wiley.com/doi/10.1002/aelm.70610 by michele bonin - Politecnico Di Torino Sist. Bibl Del Polit Di Torino , Wiley Online Library on [24/10/2026]. See the Terms and Conditions (https://onlinelibrary.wiley.com/terms-and-conditions) on Wiley Online Library for rules of use; OA articles are governed by the applicable Creative Commons License

at 700°C for 20 s in N_2 atmosphere crystallized the films into the corresponding phase.

The X-ray data are collected from the PHI 5000 Verse Probe II Electron Microscope. Deposition is achieved by AJA phase IIJ sputtering, E-beam evaporation, and ion-milling integrated system. Photolithography is performed at the John D. O'Brien Nanofabrication Laboratory, supported by the University of Southern California.

Electrical measurements were performed using a Keysight B1500 semiconductor parameter analyzer. Dynamic switching characteristics were measured using a probe-station setup connected to a Keysight B1500A semiconductor parameter analyzer equipped with the WGFMU (Waveform Generator/Fast Measurement Unit). The HZO capacitor under test was contacted through tungsten probes and connected in series with a 33 pF reference capacitor to stabilize the voltage division and suppress high-frequency artifacts. Custom voltage waveforms were generated by the WGFMU and applied directly across the device, while transient voltage responses were simultaneously recorded using a high-bandwidth Keysight InfiniiVision MSOX3104T oscilloscope (1 GHz bandwidth, 5 GSa s^{-1} sampling rate).

5.2 | Data Preprocessing and Numerical Simulations for Triangular Wave Data

Experimental transient data were analyzed in Python to extract the dynamic charge and its time derivatives from the voltage response of the linear series capacitor. From the measured voltage across this element, the instantaneous charge and current were computed, providing the full temporal evolution required for model calibration. To minimize measurement noise while preserving physical curvature and slope, the raw traces were filtered using a Savitzky–Golay algorithm, with the window length defining the temporal averaging interval and the polynomial order setting the local fitting accuracy. For most compositions, the Q–V response was averaged over 100 stable cycles. For the $Hf_{0.5}Zr_{0.5}O_2$ device, which lies close to the ferroelectric/volatile transition, approximately 10 stable and reproducible cycles were selected; nevertheless, the averaged trace still retained residual noise due to the marginal nature of this equiatomic composition. Therefore, the Q–V trace used for quantitative fitting in Figure 4b was mildly denoised and baseline-corrected before parameter extraction. This preprocessing was used only to suppress residual experimental fluctuations while preserving the loop area, remanent charge at zero bias, switching curvature, and overall hysteretic shape. The filter parameters were optimized to achieve the best trade-off between smoothing and retention of the ferroelectric switching features. Following preprocessing, a first nonlinear regression was performed in Python to identify the dominant Landau–Ginzburg–Devonshire (LGD) and dynamic coefficients and to evaluate which higher-order terms could be neglected without loss of accuracy. To avoid overparameterization, the extended LK expression was treated as the maximum model space rather than as a fixed-parameter model for every composition. In its most general form, the extended LK core contains six LGD coefficients $\alpha, \beta, \gamma, \delta, \phi, \zeta$, four coefficients for the charge-dependent dynamic resistance $R_{dyn}(Q)$, and four coefficients for the charge-dependent pseudo-inductance $L_{dyn}(Q)$, yielding a maximum of 14 active coefficients. Final composition-specific parameter sets were selected through a model-reduction procedure based on coefficient significance, free-energy consistency, and the Bayesian information criterion (BIC). Higher-order terms were retained only when they improved the information criterion and preserved the physically correct free-energy topology; otherwise, they were fixed to zero. The complete BIC-based model comparison is reported in Section S5.2. This step provided a reduced and physically consistent model basis. The key parameter governing the ferroelectric state was then refined through Cadence Spectre simulations by matching the remanent charge at zero bias with that measured experimentally under PUND excitation. Once this reference state was established, a second nonlinear regression in Python was carried out to fit the Q–V loops across all compositions, using the experimentally derived charge and voltage traces as input. Finally, all parameters were validated through dynamic co-simulations in Cadence, where the extended Landau–Khalatnikov equations were solved numerically. Although this environment entails a higher computational cost due to the direct solution of the coupled differential equations, it ensures full physical consistency between the analytical fitting, the circuit implementation, and the experimentally observed behavior. This combined workflow guarantees that the extracted parameters are both quantitatively robust and transferable to large-scale circuit simulations.

5.3 | Leakage Modeling

To isolate the leakage contribution, dedicated measurements were performed on HZO capacitors without the series linear capacitor used in the previous experiments. This configuration allowed direct access to the intrinsic conduction characteristics of the device. According to the physical derivation and analytical formulation provided in Section S3, the leakage current was modeled using a Poole–Frenkel (PF) transport mechanism. This approach is supported by experimental evidence showing field-assisted carrier emission consistent with thermionic behavior. The PF formulation was therefore adopted as the most compact and physically grounded representation of the leakage process. Following the analytical description, the final fitting model was reduced to two effective parameters that capture the essential field and temperature dependence of the leakage current, while implicitly including the underlying thermo–emission physics. These parameters were extracted through nonlinear regression in Python, using the experimentally measured current–voltage characteristics as input. The resulting compact, physics-based model efficiently reproduces the measured leakage trends over a wide temperature range, providing a quantitative link between the conduction mechanism and the overall device response.

Acknowledgments

We thank John D. O'Brien Nanofabrication Laboratory and Core Center of Excellence in Nano Imaging, supported by the University of Southern California, for their assistance with device fabrication and analysis. This work was funded by the Air Force Office of Scientific Research through the Center of Excellence (Contract No. FA9550-24-1-0322) and the National Science Foundation (Contract No. 2036359).

2199160x, 0, Downloaded from https://advanced.onlinelibrary.wiley.com/doi/10.1002/aelm.70610 by michele bonin - Politecnico Di Torino Sist. Bibl Del Polit Di Torino , Wiley Online Library on [24/10/2026]. See the Terms and Conditions (https://onlinelibrary.wiley.com/terms-and-conditions) on Wiley Online Library for rules of use; OA articles are governed by the applicable Creative Commons License

Conflicts of Interest

The authors declare no conflicts of interest.

Data Availability Statement

The data supporting the findings of this study are available from the corresponding author upon reasonable request.

References

1. G. Indiveri and S.-C. Liu, "Memory and Information Processing in Neuromorphic Systems," *Proceedings of the IEEE* 103, no. 8 (2015): 1379–1397, https://doi.org/10.1109/JPROC.2015.2444094.

2. C. Mead, "Neuromorphic Electronic Systems," *Proceedings of the IEEE* 78, no. 10 (1990): 1629–1636, https://doi.org/10.1109/5.58356.

3. J. F. Scott and C. A. Paz de Araujo, "Ferroelectric Memories," *Science* 246, no. 4936 (1989): 1400–1405, https://doi.org/10.1126/science.246.4936.1400.

4. S. Oh, H. Hwang, and I. K. Yoo, "Ferroelectric Materials for Neuromorphic Computing," *APL Materials* 7, no. 9 (2019): 091109, https://doi.org/10.1063/1.5108562.

5. S. Salahuddin and S. Datta, "Use of Negative Capacitance to Provide Voltage Amplification for Low Power Nanoscale Devices," *Nano Letters* 8, no. 2 (2008): 405–410, https://doi.org/10.1021/nl071804g.

6. A. I. Khan, K. Chatterjee, B. Wang, et al., "Negative Capacitance in a Ferroelectric Capacitor," *Nature Materials* 14, no. 2 (2015): 182–186, https://doi.org/10.1038/nmat4148.

7. U. Schroeder, C. S. Hwang, and H. Funakubo, *Ferroelectricity in Doped Hafnium Oxide: Materials, Properties and Devices* (Woodhead Publishing, 2025).

8. Z. Zhang, G. Tian, J. Huo, et al., "Recent Progress of Hafnium Oxide-Based Ferroelectric Devices for Advanced Circuit Applications," *Science China Information Sciences* 66, no. 10 (2023): 200405, https://doi.org/10.1007/s11432-023-3780-7.

9. T. Mikolajick, M. H. Park, L. Begon-Lours, and S. Slesazeck, "From Ferroelectric Material Optimization to Neuromorphic Devices," *Advanced Materials* 35, no. 37 (2023): 2206042, https://doi.org/10.1002/adma.202206042.

10. K. Ni, J. A. Smith, B. Grisafe, et al., "SoC Logic Compatible Multi-Bit FeMFET Weight Cell for Neuromorphic Applications," in *2018 IEEE International Electron Devices Meeting (IEDM)* (IEEE, 2018), 13.2.1–13.2.4.

11. T. Wang, J. Meng, X. Zhou, et al., "Reconfigurable Neuromorphic Memristor Network for Ultralow-Power Smart Textile Electronics," *Nature Communications* 13, no. 1 (2022): 7432.

12. T. S. Böscke, J. Müller, D. Bräuhaus, U. Schröder, and U. Böttger, "Ferroelectricity in Hafnium Oxide Thin Films," *Applied Physics Letters* 99, no. 10 (2011): 102903, https://doi.org/10.1063/1.3634052.

13. J. Muller, T. S. Boscke, U. Schroder, et al., "Ferroelectricity in Simple Binary ZrO2 and HfO2," *Nano Letters* 12, no. 8 (2012): 4318–4323, https://doi.org/10.1021/nl302049k.

14. Z. Li, T. Wang, J. Yu, et al., "Ferroelectric Hafnium Oxide Films for in-Memory Computing Applications," *Advanced Electronic Materials* 8, no. 12 (2022): 2200951, https://doi.org/10.1002/aelm.202200951.

15. U. Schroeder, M. H. Park, T. Mikolajick, and C. S. Hwang, "The Fundamentals and Applications of Ferroelectric HfO_2," *Nature Reviews Materials* 7, no. 8 (2022): 653–669, https://doi.org/10.1038/s41578-022-00443-y.

16. M. H. Park, Y. H. Lee, T. Mikolajick, U. Schroeder, and C. S. Hwang, "Review and Perspective on Ferroelectric HfO_2-Based Thin Films for Memory Applications," *MRS Communications* 8, no. 3 (2018): 795–808, https://doi.org/10.1557/mrc.2018.175.

17. Y. Wang, L. Tao, R. Guzman, et al., "A stable Rhombohedral Phase in Ferroelectric $Hf(Zr)_{1+x}O_2$ Capacitor with Ultralow Coercive Field," *Science* 381, no. 6657 (2023): 558–563, https://doi.org/10.1126/science.adf6137.

18. A. K. Jonscher, "The Physical Origin of Negative Capacitance," *Journal of the Chemical Society, Faraday Transactions 2: Molecular and Chemical Physics* 82, no. 1 (1986): 75–81, https://doi.org/10.1039/F29868200075.

19. C.-H. Liu, K.-Y. Hsiang, Z.-X. Li, et al., "Nonvolatile and Volatile Memory Fusion of Antiferroelectric-like Hafnium–Zirconium Oxide for Multi-Bit Access and Endurance $>10^{12}$ Cycles by Alternating Polarity Cycling Recovery and Spatially Resolved Evolution," *ACS Applied Materials and Interfaces* 17, no. 9 (Mar 2025): 14342–14349, https://doi.org/10.1021/acsami.4c14132.

20. H. Dahlberg, A. E. O. Persson, R. Athle, and L.-E. Wernersson, "Ferroelectric-Antiferroelectric Transition of Hfl–xZrxO2 on Indium Arsenide with Enhanced Ferroelectric Characteristics for Hf0.2Zr0.8O2," *ACS Applied Electronic Materials* 4, no. 12 (Dec 2022): 6357–6363, https://doi.org/10.1021/acsaelm.2c01483.

21. J. F. Ihlefeld, S. T. Jaszewski, and S. S. Fields, "A Perspective on Ferroelectricity in Hafnium Oxide: Mechanisms and Considerations Regarding its Stability and Performance," *Applied Physics Letters* 121, no. 24 (2022): 240502, https://doi.org/10.1063/5.0129546.

22. P. D. Lomenzo, M. Materano, T. Mittmann, et al., "Harnessing Phase Transitions in Antiferroelectric ZrO2 Using the Size Effect," *Advanced Electronic Materials* 8, no. 1 (2022): 2100556, https://doi.org/10.1002/aelm.202100556.

23. P. D. Lomenzo, L. Collins, R. Ganser, et al., "Discovery of Nanoscale Electric Field-Induced Phase Transitions in ZrO2," *Advanced Functional Materials* 33, no. 41 (2023): 2303636, https://doi.org/10.1002/adfm.202303636.

24. S. Asapu, T. Moon, K. Mahalingam, et al., "Accurate Compact Nonlinear Dynamical Model for a Volatile Ferroelectric ZrO_2 Capacitor," *npj Unconventional Computing* 1, no. 1 (2024): 7, https://doi.org/10.1038/s44335-024-00007-z.

25. F. Zhang, Z.-D. Luo, Q. Yang, et al., "Evolution of the Interfacial Layer and its Impact on Electric-Field-Cycling Behaviors in Ferroelectric $Hf_{1-x}Zr_xO_2$," *ACS Applied Materials and Interfaces* 14, no. 8 (2022): 11028–11037, https://doi.org/10.1021/acsami.1c22426.

26. B. Sun, J. Zhang, J. Meng, and T. Wang, "Low Power Optoelectronic Neuromorphic Memristor for In-Sensor Computing and Multi-level Hardware Security Communications," *Advanced Science* 13 (2026): e24299.

27. Z. Wang, J. Zhang, Z. Zhang, J. Meng, C. Lei, and T. Wang, "Near-Sensor Neuromorphic Computing System Based on a Thermopile Infrared Detector and a Memristor for Encrypted Visual Information Transmission," *Nano Letters* 25, no. 19 (2025): 8049–8057.

28. L. D. Landau and I. M. Khalatnikov, "On the Anomalous Absorption of Sound near a Second Order Phase Transition Point," *Doklady Akademii Nauk SSSR* 96 (1954), 469–472.

29. S. Sivasubramanian, A. Widom, and Y. Srivastava, "Equivalent Circuit and Simulations for the Landau-Khalatnikov Model of Ferroelectric Hysteresis," *IEEE Transactions on Ultrasonics, Ferroelectrics, and Frequency Control* 50, no. 8 (2003): 950–957, https://doi.org/10.1109/TUFFC.2003.1226538.

30. M. Segatto, F. Rupil, and D. Esseni, "Analytical Procedure for the Extraction of Material Parameters in Antiferroelectric ZrO2," *IEEE Transactions on Electron Devices* 70, no. 6 (2023): 3037–3042, https://doi.org/10.1109/TED.2023.3265626.

31. P.-H. Cheng, Y.-T. Yin, I.-N. Tsai, et al., "Negative Capacitance From the Inductance of Ferroelectric Switching," *Communications Physics* 2, no. 1 (2019): 32, https://doi.org/10.1038/s42005-019-0120-1.

32. S. Jo, H. Lee, D.-H. Choe, et al., "Negative Differential Capacitance in Ultrathin Ferroelectric Hafnia," *Nature Electronics* 6, no. 5 (2023): 390–397, https://doi.org/10.1038/s41928-023-00959-3.

2199160x, 0, Downloaded from https://advanced.onlinelibrary.wiley.com/doi/10.1002/aelm.70610 by michele bonin - Politecnico Di Torino Sist. Bibl Del Polit Di Torino , Wiley Online Library on [24/10/2026]. See the Terms and Conditions (https://onlinelibrary.wiley.com/terms-and-conditions) on Wiley Online Library for rules of use; OA articles are governed by the applicable Creative Commons License

33. H. W. Park, J. Roh, Y. B. Lee, and C. S. Hwang, "Modeling of Negative Capacitance in Ferroelectric Thin Films," *Advanced Materials* 31, no. 32 (2019): e1805266, https://doi.org/10.1002/adma.201805266.

34. E. Paasio, M. Prunnila, and S. Majumdar, "Modelling Ferroelectric Hysteresis of HZO Capacitor with Jiles-Atherton Model for Non-Volatile Memory Applications," in *2023 IEEE 12th Non-Volatile Memory Systems and Applications Symposium (NVMSA)* (IEEE, 2023), 1–2.

35. S. Sugathan, K. Thekkepat, S. Bandyopadhyay, J. Kim, and P.-R. Cha, "A Phase Field Model Combined with a Genetic Algorithm for Polycrystalline Hafnium Zirconium Oxide Ferroelectrics," *Nanoscale* 14, no. 40 (2022): 14997–15009, https://doi.org/10.1039/D2NR02678C.

36. K. Ni, M. Jerry, J. A. Smith, and S. Datta, "A Circuit Compatible Accurate Compact Model for Ferroelectric-FETs," in *2018 IEEE Symposium on VLSI Technology* (IEEE, 2018), 131–132.

37. H. H. Huang, C. Y. Cho, T. Y. Lin, et al., "Modeling Fatigue-Breakdown Dilemma in Ferroelectric $Hf_{0.5}Zr_{0.5}O_2$ and Optimized Programming Strategies," in *2022 IEEE International Electron Devices Meeting (IEDM)* (IEEE, 2022), 13.5.1–13.5.4.

38. D. H. Han, S. Y. Kim, H. W. Jeong, et al., "Temperature-Dependent 111-Texture Transfer to Hf0.5Zr0.5O2 Films from 111-Textured TiN Electrode and Its Impact on Ferroelectricity," *ACS Applied Materials and Interfaces* 17, no. 18 (2025): 26836–26844, https://doi.org/10.1021/acsami.4c17978.

39. S. Shi, H. Xi, T. Cao, et al., "Interface-Engineered Ferroelectricity of Epitaxial Hf0.5Zr0.5O2 Thin Films," *Nature Communications* 14, no. 1 (Mar 2023): 1780, https://doi.org/10.1038/s41467-023-37560-3.

40. D. Wang, Y. Zhang, Y. Guo, Z. Shang, F. Fu, and X. Lu, "Impact of Annealing Temperature on the Ferroelectric Properties of W/Hf0.5Zr0.5O2/W Capacitor," *Chinese Physics B* 32, no. 9 (aug 2023): 097701, https://doi.org/10.1088/1674-1056/aca9c6.

41. H. A. Hsain, Y. Lee, S. Lancaster, et al., "Reduced Fatigue and Leakage of Ferroelectric TiN/Hf0.5Zr0.5O2/TiN Capacitors by Thin Alumina Interlayers at the Top or Bottom Interface," *Nanotechnology* 34, no. 12 (jan 2023): 125703, https://doi.org/10.1088/1361-6528/acad0a.

42. Mohit, T. Miyasako, and E. Tokumitsu, "Indium Oxide and Indium-Tin-Oxide Channel Ferroelectric Gate Thin Film Transistors with Yttrium Doped Hafnium-Zirconium Dioxide Gate Insulator Prepared by Chemical Solution Process," *Japanese Journal of Applied Physics* 60, no. SB (jan 2021): SBBM02, https://doi.org/10.35848/1347-4065/abd6da.

43. Y. Xu, D. Rossetti, S. Asapu, et al., "Volatile and Non-Volatile Ferroelectric HZO for Low-Power Reservoir Computing," *Advanced Materials Technologies* n/a, no. n/a (2026): e71125, https://doi.org/10.1002/admt.71125.

44. Y. Ishibashi, "Theory of Nonlinear Response," *Ferroelectrics* 236, no. 1 (2000): 71–79, https://doi.org/10.1080/00150190008016042.

45. X. Cheng, C. Zhou, B. Lin, et al., "Leakage Mechanism in Ferroelectric Hf0.5Zr0.5O2 Epitaxial Thin Films," *Applied Materials Today* 32 (2023): 101804, https://doi.org/10.1016/j.apmt.2023.101804.

46. H. A. Hsain, Y. Lee, S. Lancaster, et al., "Reduced Fatigue and Leakage of Ferroelectric TiN/Hf0.5Zr0.5O2/TiN Capacitors by Thin Alumina Interlayers at the Top or Bottom Interface," *Nanotechnology* 34, no. 12 (2023): 125703, https://doi.org/10.1088/1361-6528/acad0a.

47. R. Ongaro and A. Pillonnet, "Synthetic Theory of Poole and Poole-Frenkel (PF) Effects," *IEE Proceedings A (Science, Measurement and Technology)* 138, no. 2 (1991): 127–137, https://doi.org/10.1049/ip-a-3.1991.0018.

48. H. A. Hsain, Y. Lee, G. Parsons, and J. L. Jones, "Compositional Dependence of Crystallization Temperatures and Phase Evolution in Hafnia-Zirconia (HfxZr1- x) O2 Thin Films," *Applied Physics Letters* 116, no. 19 (2020): 192903, https://doi.org/10.1063/5.0002835.

49. S. Abdulazhanov, M. Lederer, D. Lehninger, T. Ali, R. Olivo, and T. Kämpfe, "The Effect of Temperature on the Ferroelectric Properties of Hafnium Zirconium Oxide MFM Thin-Film Varactors," in *2021 IEEE International Symposium on Applications of Ferroelectrics (ISAF)* (IEEE, 2021), 1–4.

50. M. Zielinski and M. Samoc, "An Investigation of the Poole-Frenkel Effect by the Thermally Stimulated Current Technique," *Journal of Physics D: Applied Physics* 10, no. 8 (1977): L105–L107, https://doi.org/10.1088/0022-3727/10/8/004.

51. H. H. Poole, "VIII. On the Dielectric Constant and Electrical Conductivity of Mica in Intense Fields," *The London, Edinburgh, and Dublin Philosophical Magazine and Journal of Science* 32, no. 187 (1916): 112–129, https://doi.org/10.1080/14786441608635546.

52. J. Frenkel, "On Pre-Breakdown Phenomena in Insulators and Electronic Semi-Conductors," *Physical Review* 54, no. 8 (1938): 647, https://doi.org/10.1103/PhysRev.54.647.

53. C. B. Sawyer and C. H. Tower, "Rochelle Salt as a Dielectric," *Physical Review* 35, no. 3 (1930): 269, https://doi.org/10.1103/PhysRev.35.269.

54. A. K. Tagantsev, L. E. Cross, and J. Fousek, *Domains in Ferroic Crystals and Thin Films*, Vol. 13 (Springer, 2010).

55. Y. Oshima, T. Takenobu, J. Pu, et al., "A Memristive Oscillator," *Advanced Physics Research* 3, no. 4 (2024): 2300117, https://doi.org/10.1002/apxr.202300117.

56. M. Itoh and L. O. Chua, "Memristor Oscillators," *International Journal of Bifurcation and Chaos* 18, no. 11 (2008): 3183–3206, https://doi.org/10.1142/S0218127408022354.

57. B. Muthuswamy and L. O. Chua, "Simplest Chaotic Circuit," *International Journal of Bifurcation and Chaos* 20, no. 05 (2010): 1567–1580, https://doi.org/10.1142/S0218127410027076.

58. Y. Li, J. Li, R. Liang, et al., "Switching Dynamics of Ferroelectric HfO2-ZrO2 with Various ZrO2 Contents," *Applied Physics Letters* 114, no. 14 (2019): 142902, https://doi.org/10.1063/1.5093793.

59. M. Si, X. Lyu, P. R. Shrestha, et al., "Ultrafast Measurements of Polarization Switching Dynamics on Ferroelectric and Anti-Ferroelectric Hafnium Zirconium Oxide," *Applied Physics Letters* 115, no. 7 (2019): 072107, https://doi.org/10.1063/1.5098786.

60. H. Dahlberg and L.-E. Wernersson, "Dynamics of Polarization Switching in Mixed Phase Ferroelectric-Antiferroelectric HZO Thin Films," in *ESSDERC 2023-IEEE 53rd European Solid-State Device Research Conference (ESSDERC)* (IEEE, 2023), 33–36.

61. Y. Peng, W. Xiao, G. Zhang, G. Han, Y. Liu, and Y. Hao, "Synaptic Behaviors in Ferroelectric-Like Field-Effect Transistors with Ultrathin Amorphous HfO2 Film," *Nanoscale Research Letters* 17, no. 1 (2022): 17, https://doi.org/10.1186/s11671-022-03655-x.

62. C.-M. Song, D. Kim, S. Lee, and H.-J. Kwon, "Ferroelectric 2D SnS2 Analog Synaptic FET," *Advanced Science* 11, no. 16 (2024): 2308588, https://doi.org/10.1002/advs.202308588.

63. R. Cao, X. Zhang, S. Liu, et al., "Compact Artificial Neuron Based on Anti-Ferroelectric Transistor," *Nature Communications* 13, no. 1 (2022): 7018, https://doi.org/10.1038/s41467-022-34774-9.

64. B. Suresh, M. Bertele, E. T. Breyer, et al., "Simulation of Integrate-and-Fire Neuron Circuits Using HfO2-Based Ferroelectric Field Effect Transistors," in *2019 26th IEEE International Conference on Electronics, Circuits and Systems (ICECS)* (IEEE, 2019), 229–232.

65. S. Dutta, C. Schafer, J. Gomez, K. Ni, S. Joshi, and S. Datta, "Supervised Learning in all FeFET-Based Spiking Neural network: Opportunities and Challenges," *Frontiers in Neuroscience* 14 (2020): 634, https://doi.org/10.3389/fnins.2020.00634.

66. S. Rai, S. Srinivasa, P. Cadareanu, et al., "Emerging Reconfigurable Nanotechnologies: Can They Support Future Electronics?," in *2018 IEEE/ACM International Conference on Computer-Aided Design (ICCAD)* (IEEE, 2018), 1–8.

67. A. Ram, K. Maity, C. Marchand, et al., "Reconfigurable Multifunctional van der Waals Ferroelectric Devices and Logic Circuits," *ACS Nano* 17, no. 21 (2023): 21865–21877, https://doi.org/10.1021/acsnano.3c07952.

2199160x, 0, Downloaded from https://advanced.onlinelibrary.wiley.com/doi/10.1002/aelm.70610 by michele bonin - Politecnico Di Torino Sist. Bibl Del Polit Di Torino , Wiley Online Library on [24/10/2026]. See the Terms and Conditions (https://onlinelibrary.wiley.com/terms-and-conditions) on Wiley Online Library for rules of use; OA articles are governed by the applicable Creative Commons License

68. Z. Zhao, J. Kang, A. Tunga, et al., "Content-Addressable Memories and Transformable Logic Circuits Based on Ferroelectric Reconfigurable Transistors for In-Memory Computing," *ACS Nano* 18, no. 4 (2024): 2763–2771, https://doi.org/10.1021/acsnano.3c03900.

69. J. Niu, D. Kim, J. Li, J. Lyu, Y. Lee, and S. Lee, "Reconfigurable Sequential-Logic-in-Memory Implementation Utilizing Ferroelectric Field-Effect Transistors," *ACS Nano* 19, no. 5 (2025): 5493–5502, https://doi.org/10.1021/acsnano.4c14062.

70. M. Hoffmann, Z. Wang, N. Tasneem, et al., "Antiferroelectric Negative Capacitance From a Structural Phase Transition in Zirconia," *Nature Communications* 13, no. 1 (2022): 1228, https://doi.org/10.1038/s41467-022-28860-1.

71. J. K. Wang, C. VanEssen, N. Yang, et al., "Toward a GHz-Frequency BEOL Ferroelectric Negative-Capacitance Oscillator With a Wide Tuning Range," *IEEE Transactions on Nanotechnology* 23 (2024): 591–599, https://doi.org/10.1109/TNANO.2024.3430221.

72. Z. Chen, W. Li, Z. Fan, et al., "All-Ferroelectric Implementation of Reservoir Computing," *Nature Communications* 14, no. 1 (2023): 3585, https://doi.org/10.1038/s41467-023-39371-y.

73. J. Kim, E. C. Park, W. Shin, et al., "Analog Reservoir Computing via Ferroelectric Mixed Phase Boundary Transistors," *Nature Communications* 15, no. 1 (2024): 9147, https://doi.org/10.1038/s41467-024-53321-2.

Supporting Information

Additional supporting information can be found online in the Supporting Information section.

Supporting File: aelm70610-sup-0001-SuppMat.pdf.

2199160x, 0, Downloaded from https://advanced.onlinelibrary.wiley.com/doi/10.1002/aelm.70610 by michele bonin - Politecnico Di Torino Sist. Bibl Del Polit Di Torino , Wiley Online Library on [24/10/2026]. See the Terms and Conditions (https://onlinelibrary.wiley.com/terms-and-conditions) on Wiley Online Library for rules of use; OA articles are governed by the applicable Creative Commons License